PAPER • OPEN ACCESS

Impact of drift flows and turbulence on island divertor operation in Wendelstein 7-X

To cite this article: Carsten Killer *et al* 2026 *Nucl. Fusion* **66** 056031

OPEN ACCESS
IOP Publishing | International Atomic Energy Agency Nuclear Fusion
Nucl. Fusion **66** (2026) 056031 (14pp) https://doi.org/10.1088/1741-4326/ae5e91

Impact of drift flows and turbulence on island divertor operation in Wendelstein 7-X

Carsten Killer[1,*], Dario Cipciar[1], Arun Pandey[2], Valeria Perseo[1], Floris Scharmer[1], Seung Gyou Baek[3], Olaf Grulke[1,4], David Matthew Kriete[5], Felix Reimold[1], Adrian von Stechow[1] and the W7-X Team[a]

[1] Max-Planck-Institut für Plasmaphysik, Wendelsteinstr. 1, Greifswald, 17491, Germany
[2] Department of Nuclear Engineering and Engineering Physics, University of Wisconsin-Madison, Madison, WI, United States of America
[3] Massachusetts Institute of Technology—Plasma Science and Fusion Center, Cambridge, MA 02139, United States of America
[4] Department of Physics, Technical University of Denmark, Lyngby, Denmark
[5] Auburn University, Auburn, AL, United States of America

E-mail: carsten.killer@ipp.mpg.de

Received 29 January 2026, revised 19 March 2026
Accepted for publication 13 April 2026
Published 23 April 2026

Abstract

The island divertor in Wendelstein 7-X employs a chain of stationary magnetic islands to separate the confined plasma from the divertor targets. In this configuration, the scrape-off layer (SOL) exhibits complex patterns of counter-propagating bi-normal $E \times B$ plasma flows with typical velocities of a few km s^{-1}. Due to the long parallel connection length in the island divertor, such flows can well compete or dominate parallel transport on the open field lines to the divertor targets, which could significantly alter heat and particle flux patterns. Reversed field experiments clearly indicate an important role of drift flows for density distributions in the SOL and at the divertor. These effects cannot be reproduced by state-of-the-art models such as EMC3-EIRENE, where drift flow physics is not yet included. The mismatch between experiment and simulation poses a critical challenge in predicting heat loads for optimizing W7-X divertor operation at higher heating powers, and for the design of future stellarator reactors. In a separatrix plasma density scan in attached plasmas, a complex picture emerges: drift flow velocities decrease slightly towards higher densities, and divertor heat loads become more up-down symmetric. However, the density distributions in the SOL and at the divertor still diverge from expectations. The role of turbulent transport as another cross-field transport mechanism in this context is explored.

[a] See Grulke *et al* 2024 (https://doi.org/10.1088/1741-4326/ad2f4d) for the W7-X Team.
[*] Author to whom any correspondence should be addressed.

Keywords: stellarator, scrape-off layer, drift flows, island divertor

(Some figures may appear in colour only in the online journal)

1. Introduction

Stellarators are recently emerging as increasingly promising magnetic confinement fusion concepts, with the optimized stellarator Wendelstein 7-X (W7-X) currently exploring the path towards reactor-relevant scenarios. The most mature exhaust concept for stellarators is the island divertor, which was tested in W7-AS [1, 2] and is now in operation in W7-X [3]. In W7-X, the vacuum magnetic field is designed such that a stationary chain of resonant magnetic islands exists at the plasma edge, separating the confined plasma from the divertor targets. In W7-X, there are 4, 5, or 6 islands per poloidal cross-section depending on the chosen magnetic configuration and the associated resonance of the rotational transform. The diverting magnetic field of the islands has a very small pitch angle ($\sim 10^{-3}$) [4], resulting in parallel connection lengths to the divertor targets of several 100 m. As the targets are toroidally discontinuous, shadowed regions of very short connection length exist in between the targets (TSR: *Target Shadow Region*). These regions are filled with particles and energy by perpendicular transport through the islands or the private flux region [4, 5] and have no equivalent in axisymmetric tokamak divertors.

The two main perpendicular transport processes in the island divertor scrape-off layer (SOL) are bi-normal drift flows and radial turbulent transport. Bi-normal drift flows have been observed experimentally [6–8] and have been identified to cause significant asymmetries between upper and lower divertors [9, 10], complex modifications of the parallel flow structures [9], and are linked to non-monotonic radial electron temperature profiles [7, 11]. In these initial investigations, the impact of drift flows appears to decrease for higher plasma densities. In addition, radial drift flows from poloidal electric fields are conceivable [9], but have not been experimentally identified yet. Turbulent radial transport has been observed in W7-X [12, 13] but appears to only have a moderate effect so far [14]. The strong increase of turbulent transport at high SOL densities known in tokamaks [15] has not been reported in W7-X so far. Due to the intricate SOL geometry of the island divertor, perpendicular SOL transport affects heat and particle exhaust to the divertor in a complex fashion and is presumably responsible for recent observations of unexpected heat loads to vulnerable plasma-facing components as W7-X develops towards higher heating powers [16, 17].

To date, many of these observations cannot be fundamentally reproduced with numerical models: most edge transport models for fusion plasmas are two-dimensional and rely on the axisymmetry of tokamaks. While several models are currently being developed towards stellarators [18–20], to date the only established 3D plasma-neutral edge transport code capable of simulating the 3D island divertor geometry of W7-X is EMC3-EIRENE [21]. However, it does not self-consistently treat perpendicular turbulent transport, and does not include drifts such as $E \times B$ or diamagnetic drifts. As a consequence, no detailed global match of simulation results with experiments is readily achieved [22, 23], although specific questions can be well addressed [21, 24–27]. This situation is a critical issue for the development of future reactor-relevant stellarator divertor concepts—an activity which relies on validated models.

In this paper, an overview of recent experimentally observed drift effects and their implications for divertor operation in W7-X is given. While previous reports focused on the comparison of forward and reversed magnetic field experiments in the *Low Iota* configuration [9, 10] with a 5/6 edge island chain (which has a particularly small pitch angle and thus expects strongest effect of drifts [27]), we now investigate the (more relevant) *Standard* and *High Mirror* configurations. Both configurations feature a 5/5 island chain with larger pitch angle than *Low Iota*. The majority of W7-X experiments are conducted in these configurations, as they exhibit better core plasma confinement, and the divertor shape is optimized towards long pulse operation in both of these configurations. Furthermore, *Standard* configuration has the best divertor diagnostic coverage, while *High Mirror* configuration is the nominal optimization point of W7-X in terms of reduced bootstrap current and fast particle losses [28]. A comparison of the SOL structure of both configurations is given in the appendix A.1.

Further, the role of plasma density on drift flows is explored. Previous investigations mostly found strong drift flow effects at low densities but smaller effects towards high densities [9, 11]. The density dependence is important as reactor-relevant scenarios run at high plasma density. Finally, we explore the role of turbulent transport in the SOL as another transport channel that might become increasingly relevant at high plasma densities and high heating powers [17].

2. The island divertor SOL geometry and its effect on plasma transport

Perpendicular transport by drifts follows from the gradients of plasma temperature, density, and electric potential and back-react on the plasma conditions, resulting in a self-consistent equilibrium. All ingredients of this equilibrium depend on the 3D geometry of the island divertor SOL. The geometry of the magnetic *Standard configuration* is introduced in figure 1, where in the 3D sketch in a) the islands are shown as colored ribbons that surround the main plasma (blue). The divertor modules (black) intersect the magnetic islands at discrete toroidal positions. The principal directions for plasma transport are indicated both in the 3D plot in figure 1(*a*), in the example Poincare cross section in figure 1(*b*), and in the divertor region close-up figures in figure 1(*c*) : parallel to the magnetic field (dark blue), bi-normal/poloidal on the island flux surfaces (green), and radially across the island, perpendicular to the last closed flux surface (LCFS) (red).

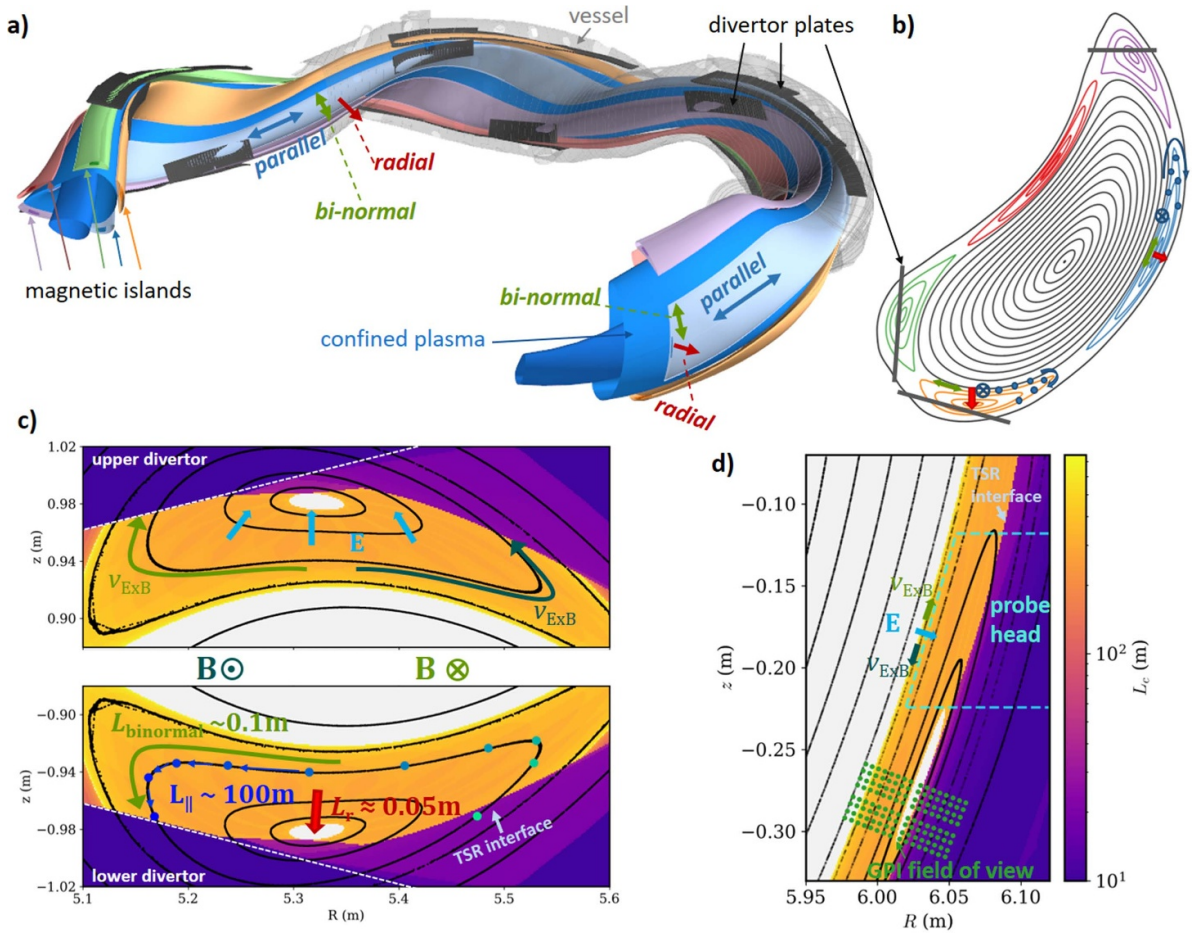

Figure 1. W7-X geometry in the *Standard* magnetic configuration. (*a*) 3D sketch. For clarity, individual components are not shown over the full toroidal extent. (*b*) Poincare cross section showing the flux surfaces of the main plasma (black), the five magnetic islands (colored), and divertor targets (gray). For two islands, the principal geometric directions from (*a*) are sketched. (*c*) Close-up of an upper and lower divertor region with Poincare plot (black) and connection lengths to the divertor color-coded. For the lower divertor, the typical length scales of the principal geometric directions from (*a*) and intersection points from multiple toroidal turns of one field line (circles) are included. For the upper divertor, the $E \times B$ flow mechanism is sketched. (*d*) Similar figure as (*c*) for the outboard mid-plane of the cross-section from (*b*), where the reciprocating probe and gas puff imaging are installed.

For the parallel direction, the individual markers on the selected island flux surfaces in figure 1(*b*) indicate the intersection points after one full toroidal turn of the field line. Due to the rotational transform $\iota/2\pi = 1$, the field line stays in the same island and ends up slightly displaced on its flux surface. This small poloidal displacement is approximately given by $2\pi R\Theta$ where R is the major radius and Θ is the island magnetic pitch angle, which is on the order of 10^{-3} in W7-X, i.e. much smaller than in tokamaks where $\Theta \sim 10^{-1}$ [4, 29].

The principal directions in figure 1 are associated with very different scale lengths regarding the proximity to divertor targets. This is highlighted in figure 1(*c*), which shows a close-up view of lower and upper divertor regions and, in addition to the Poincare plot, presents the magnetic connection length to the targets color-coded. Starting from a position close to the LCFS, it takes a field line several multiple toroidal turns, i.e. several 100 m, to reach the divertor plate. The intersection points of one field line in the island in the given cross section are indicated by the (blue to cyan) circles. Traveling perpendicular to the magnetic field on that same flux surface, i.e. in the bi-normal direction, the distance is just a few 0.1 m (green). This transport direction would be invoked by $E \times B$ drifts of particles if electric fields were perpendicular to the magnetic island flux surfaces, i.e. constant electric potential on island flux surfaces. We note that this assumption is overly simplified and would lead to a complete domination of drift flow heat transport over parallel heat transport [23].

Still, non-monotonic radial electric fields across the islands and associated bi-normal $E \times B$ flows have repeatedly been reported in W7-X with typical (measured or inferred) flow velocities of some km s^{-1} [6–8, 11]. In some cases in [7], the electric potential aligned locally with island flux surfaces, but the global picture remains unclear as all relevant diagnostics only cover individual parts of the island. In particular, it is not clear whether the $E \times B$ flows circulate fully around the flux surfaces of each island, or whether they cross the X-points between different islands. Still, effects of the observed $E \times B$

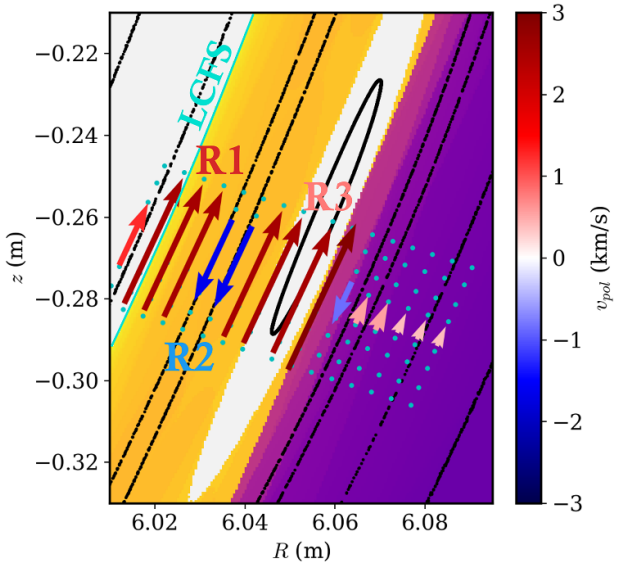

Figure 2. (*a*) Typical bi-normal velocity pattern measured by GPI (quiver plot) in magnetic *Standard* configuration for program 20241210.45. In the background, the magnetic structure including the connection length to the targets is plotted (same connection length colorbar as figure 1(*d*)).

flows agreeing with the simplified picture in figure 1(*c*) manifest as up-down asymmetries in divertor heat fluxes [10] and radiation distribution [30], and modification of the parallel flow structures [9]. As sketched in the upper divertor view of figure 1(*c*), the drift flow points either directly towards the target or into the TSR, depending on the magnetic field direction. The TSR corresponds to the purple part on the right hand side of figure 2 and has short connection lengths of ∼10 m as it is in the shadow between two discrete divertor modules. Hence, it has no parallel connection to the separatrix region, and is filled only via perpendicular transport through the TSR interface in the islands or the private flux region. In earlier field reversal experiments in the *Low Iota* configuration, a particularly strong change of divertor loads associated to the TSR have been observed, indicating a major role of drift effects in filling the TSR [9, 10]. Further, local maxima of electron temperature peaks have been repeatedly reported at the boundary of TSR and main SOL [7, 11, 31, 32].

Finally, in the direction normal to the LCFS, the distance to the target is just some cm (red in figure 1). This transport channel would be most effective in terms of the short physical distance to the target, but has typically much lower particle fluxes: Turbulent transport is found to lead to rather low diffusion coefficients of $D_\perp = 0.2\ \mathrm{m^2\ s^{-1}}$ in W7-X [14] which is smaller than the widely assumed values of $D_\perp = 0.5\ \mathrm{m^2\ s^{-1}}$ [21] to $D_\perp = 1\ \mathrm{m^2\ s^{-1}}$ [25]. Recent simulations have shown that small diffusion coefficients of $D_\perp = 0.2\ \mathrm{m^2\ s^{-1}}$ can also explain certain features from experiments [22], but no global agreement between experiment and simulation is reached with either value of $D_\perp$ [23]. Furthermore, SOL turbulence in W7-X does not exhibit intermittent radial transport of blob-filaments that is known from tokamaks [13, 14, 33]. Radial $E \times B$ drifts from poloidal electric fields [9] are conceivable but have not been experimentally identified yet [7].

3. Direct observation of drift flows

The most direct observation of drift flows in W7-X is done with gas puff imaging (GPI) and reciprocating electric probes. All following experimental results are from purely electron cyclotron resonance heated (ECRH), gas-fueled hydrogen plasmas. In this default operation scenario of W7-X, core electron density profiles are predominantly flat [34]. While the separatrix density n_{sep} is the relevant quantity for SOL physics studies, it is not easily and robustly experimentally accessible in W7-X. Therefore, the line-integrated plasma density measurement from an interferometer (convertible to line-averaged density when including the interferometer chord length ≈1.3 m) is used as a reliable proxy for the n_{sep} in this paper, with typically $n_{\mathrm{sep}} \approx \int n\,\mathrm{d}l/(2.5\mathrm{m})$.

3.1. Gas puff imaging (GPI)

GPI is based on fast imaging of H_α emission from a localized gas puff [35]. Using spatio-temporal analysis, the propagation of fluctuating structures is obtained [8]. In the W7-X SOL, bi-normal flows with typical velocities of several km $\mathrm{s^{-1}}$ are observed, while radial propagation is significantly slower (to a point where it is usually not discernible at all [33]). Across the radial width of the SOL, the flows change sign, with between one to four flow reversal layers. A typical flow pattern in the magnetic *Standard* configuration of W7-X is presented in figure 2 on top of the magnetic geometry (Poincare plot and connection lengths). In the figure, the centers of the 16 × 8 (column x row) detector pixels on the image plane are shown in cyan circles, defining a regular grid of measurement locations across the SOL regions near the LCFS, the island confined region, and the TSR. Three major flow channels are found, R1 directed upwards in the main SOL (close to the LCFS), R2 directed downwards between the LCFS and the island O-point, R3 directed upwards in the O-point region of closed field lines. In the TSR, much smaller velocities are observed. The magnitude and spatial distribution of poloidal flow channels is highly sensitive to the magnetic field geometry, e.g. the size and position of magnetic islands [7, 8].

3.2. Reciprocating electric probes

A multi-pin Langmuir probe head on a reciprocating multi-purpose manipulator (MPM) provides radial profiles of electron temperature T_{e} and density n as well as the floating potential V_{f}. Using a poloidal array of in total 29 probes, the time-averaged plasma properties in a 2D region of the SOL are obtained [7]. The probe system is installed in a stellarator-symmetric cross section to GPI, with a slight vertical displacement due to technical constraints, such that the fields of view are adjacent but do not overlap [7]. A typical result in the magnetic *Standard* configuration for a plasma with heating power $P_{\mathrm{ECRH}} = 3\,\mathrm{MW}$ and line-integrated density $n_{\mathrm{dl}} = 5 \times 10^{19}\ \mathrm{m^{-2}}$ is shown in figure 3. The electron temperature T_{e} and density n profiles are measured by five triple Langmuir probes that are radially scanning the SOL at different vertical

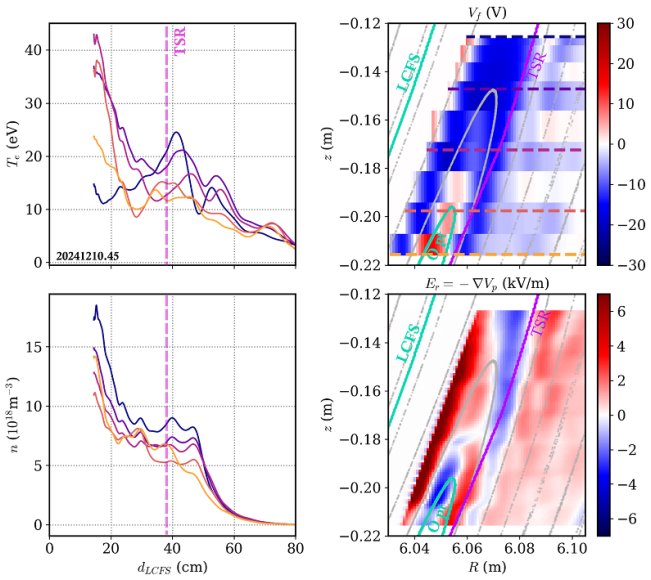

Figure 3. Left: Radial profiles of T_e, n taken by five triple Langmuir probes. Right: 2D representation of floating potential V_f from nine floating probes and radial electric field $E_r = -\nabla V_p = -\nabla(V_f + 2.8T_e)$. In addition, a Poincare plot (light gray) and two contour lines separating open from closed field lines (cyan) are shown: the LCFS and and the confined region around the island O point. The paths of the five triple probes are indicated by horizontal dashed lines. All data is low-pass filtered to 150 Hz to display the time-averaged radial profiles.

positions, see the dashed lines in figure 3 (right). Except for the uppermost probe, T_e decreases from higher values close to the LCFS and features a mostly flat region between the radial island center and the TSR, at $d_{LCFS} = 30 - 40$ mm. The density profiles are smoother than the T_e profiles and show an even clearer flat profile shape in the outer part of the island density $d_{LCFS} = 30 - 45$ mm. In the TSR, after a still flat region of almost 10 mm width, the density quickly decays with a decay length of $\approx$7 mm. The behavior of the uppermost probe is discussed in the appendix A.4.

The 2D floating potential distribution in figure 3(right), taken by 9 floating probes, follows the magnetic island geometry: Local maxima of V_f are observed inside the central island flux surfaces. Large V_f gradients are aligned with the TSR boundary in the upper half of the sampled region, particularly pronounced for the upper probes around $R = 6.08$ m (i.e. $d_{LCFS} \approx 40$ mm). Concomitantly, the T_e profiles of the upper probes feature a local maximum at this position. From the T_e and V_f data, a 2D map of the plasma potential $V_p = V_f + 2.8T_e$ is obtained, which then provides the radial electric field $E_r = -\nabla_r V_p$, see figure 3(bottom right), where r is here defined as normal to the LCFS, i.e. agnostic of the island structure. The radial electric field shows a layer of locally negative E_r and thus causes sheared bi-normal $E \times B$ flows [7]. Even though the data from figures 2(a) and 3 is from the same experiment, detailed quantitative comparison of GPI and MPM drift flows has not been possible yet, due to the fields of view not overlapping, see figure 1(d). The MPM plasma parameter profiles in figure 3 already show substantial variation of the E_r profile when comparing the upper and lower part of the MPM FoV, so the extrapolation to the GPI FoV is not obvious. Further, toroidal asymmetries might play a role, as the two diagnostics are installed in different cross sections of the machine [7].

3.3. Role of magnetic geometry

As reported in [7, 8], the distribution of electric potential and drift flows is particularly sensitive to the magnetic island position. While the islands in W7-X are created by the vacuum magnetic field from the external coils and are therefore stationary, the small (compared to tokamak plasma current) but finite bootstrap current of W7-X [36] acts on the iota profile and therefore the radial island position. Early island divertor experiments have shown that SOL plasma parameters and divertor heat loads react highly sensitively to even small changes in the island position [31, 37].

A clear example for this effect from a recent experiment (with improved diagnostic coverage compared to [31]) is presented in figure 4. In this experiment in the *High Mirror* magnetic configuration (see magnetic structure in the MPM and GPI region in figure 5(c)), the discharge was kept stable at $P_{ECRH} = 5.2$ MW, $n_{dl} = 5.0 \times 10^{19}$ m^{-2}, such that the only not equilibrated quantity is the plasma current, see figure 5(a). In this magnetic configuration, the plasma current moves the islands inwards by approximately 1.8 mm kA^{-1}. In five reciprocating probe insertions at different I_p levels, 2D maps of T_e, n, V_f, E_r were taken. All quantities show a clear reaction to the small radial island shift induced by a net plasma current change of 4 kA:

- V_f: towards higher I_p, a larger and increasingly positive peak of V_f appears in the central island flux surfaces and in a wedge-shaped region for $z > -0.15$ m. Note that in this magnetic configuration there is no closed field line region in the central island flux surfaces sampled by MPM, in contrast to figure 3 and [7].
- T_e: at low I_p, T_e profiles are radially monotonic and in the poloidal direction decrease towards more negative z positions. For higher I_p, a local T_e peak at the TSR boundary appears, which is most prominent for the upper part of the MPM sampling region. At the same time, T_e at the innermost measurement positions decreases, as the LCFS moves further radially inwards.
- E_r: For higher I_p, a wedge-shaped region of negative E_r appears in the upper part of the field of view (FoV). Both positive and negative E_r magnitudes increase for higher I_p, resulting in more shear.
- n: similar to T_e, at low I_p, n profiles are radially monotonic and in the poloidal direction decrease towards more negative z positions. For higher I_p, a strong local density peak appears at the TSR boundary for the upper z positions, while a density peak appears in the island center for the lower z positions. In contrast to T_e, the density at the innermost measurement positions increases slightly while the LCFS moves inwards. The uppermost probe shows consistently

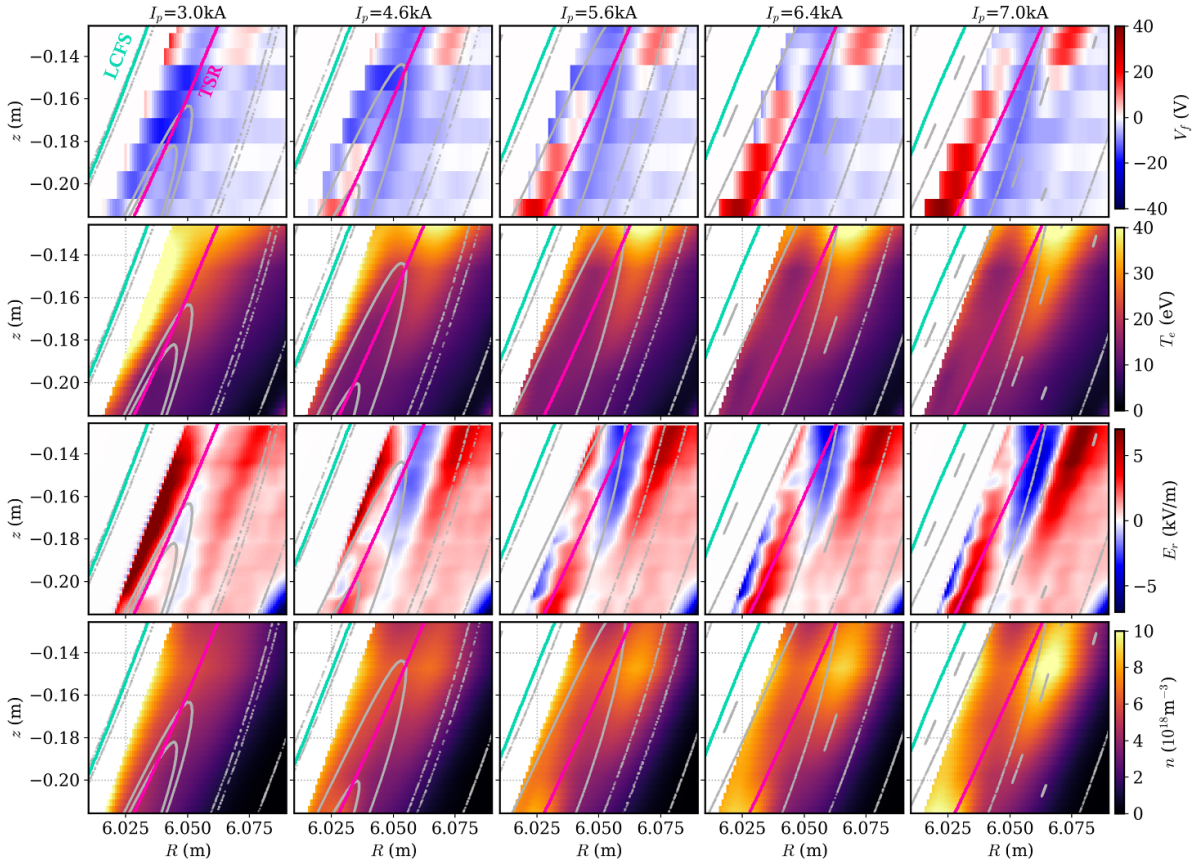

Figure 4. Reciprocating probe results from five triple probes (providing T_e, n) and nine floating probes (providing V_f) in *High Mirror* configuration in program 20241016.20. Each column corresponds to one of five probe insertions at different toroidal plasma current I_p levels, see figure 5(*a*). For each measurement, floating potential V_f, electron temperature T_e, radial electric field $E_r = -\nabla V_p$, and plasma density n are shown, each overlaid with a Poincare plot. The triple probe results are interpolated to a fine vertical grid for visual clarity and in order to calculate $V_p = V_f + 2.8T_e$

quantitatively smaller densities than the others, while the profile shape is similar, which is discussed in the appendix A.4.

In addition, three GPI measurements were taken in this experiment as indicated by the yellow markers in figure 5(*a*), with the resulting radial profiles of the bi-normal flow velocity presented in figure 5(*b*). The tendency of higher flow velocities for larger plasma currents qualitatively agrees with the E_r dependence on plasma current in figure 4. The shear layer that is visible at the innermost GPI measurement position at $I_p = 3.5$ kA leaves the FoV in the other measurements at higher I_p, as the island moves inwards while the FoV is fixed.

4. Density dependence of drift effects

Drift effects are best investigated by comparing forward and reversed magnetic field experiments. Due to the up-down symmetric modular island divertor setup, no effect of field direction is expected except for the direction of drifts (neglecting error fields, which are compensated with trim and control coils [38]). Previous investigations using forward/reversed magnetic field direction in the *Low Iota* configuration with 6 connected islands showed strongest drift flow effects at low densities and weaker effects towards higher densities [9, 10]. Here, we investigate the density dependence in the *Standard* and *High Mirror* configurations, both of which feature 5 separate edge islands. The experiment programs used for the results presented in this section are listed in A.2.

First, we consider the bi-normal flows measured by GPI. These can be identified as drift flows as their velocity flips direction upon magnetic field [8]. The role of plasma density for drift flow velocities in *Standard* configuration is presented in figure 6(*a*), where the velocities in the three regions highlighted in figure 2 are shown as a function of line-integrated plasma density. In all three regions, the flow velocity magnitude decreases towards higher plasma densities. Weaker drift flows at high plasma densities qualitatively agree with previous works reporting on the density dependence of the effects of drift flows [9, 11, 39]. However, the flow velocities are still at a level where they should substantially matter [23]. A similar trend of decreasing flow velocity magnitudes at higher densities is seen in the *High Mirror* configuration in figure 6(*b*). In the highest density dataset (orange), the flow velocities completely flips around $d_{LCFS} = 30 - 35$ mm and $d_{LCFS} = 65$ mm. This feature is not understood but occurs reproducibly across multiple independent high density

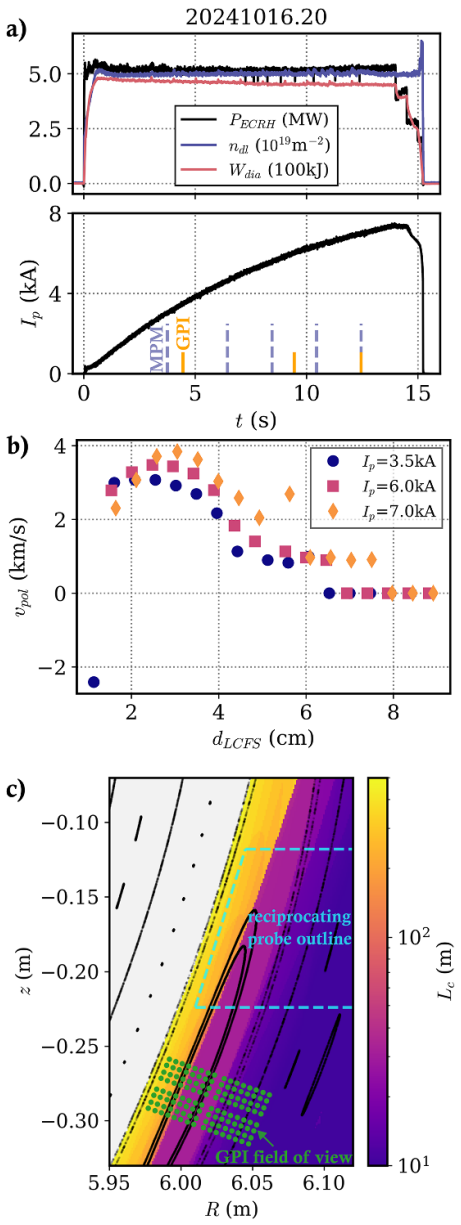

Figure 5. (*a*) Overview of experiment 20241016.20 in *High Mirror* configuration with constant heating and density but evolving toroidal plasma current I_p. Results from the five indicated MPM measurements are presented in figure 4. (*b*) Radial profiles of bi-normal flow velocity from GPI for the three measurements indicated in (*a*). (*c*) Connection lengths (color coded) and Poincare plot (black) in the GPI and MPM region in *High Mirror* configuration ($I_p = 0$).

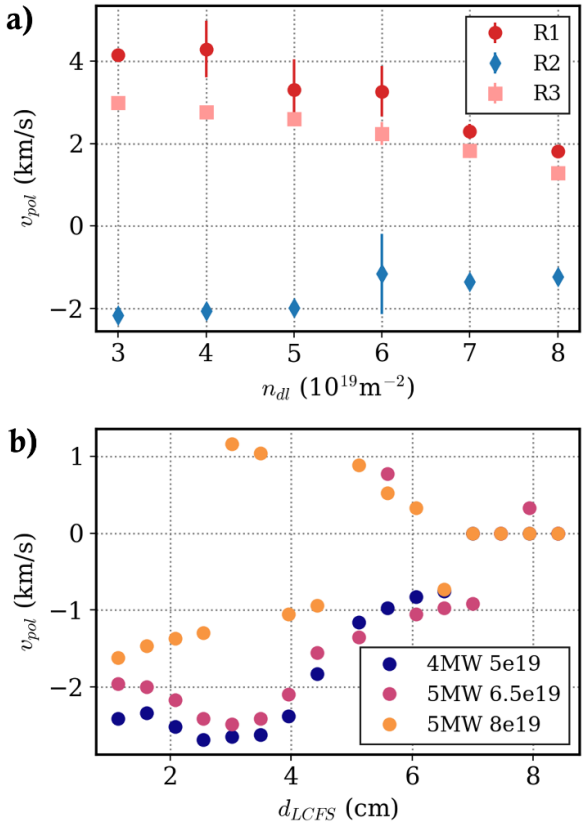

Figure 6. (*a*) Dependence of bi-normal velocity on line-integrated electron density in *Standard* configuration for the three regions R1, R2, R3 highlighted in figure 2. The error bars represent statistical scatter from averaging multiple measurements at similar experimental conditions and are often smaller than the marker size. (*b*) Flow velocity profiles for three different core densities in *High Mirror* configuration in reversed field direction.

experiments in the *High Mirror* configuration, and might indicate finite plasma β effects on the island structure.

4.1. SOL profiles - Standard configuration

SOL profiles of T_e, n, E_r in the magnetic *Standard* configuration have been measured with the MPM reciprocating probe in forward and reversed magnetic field direction, see figure 7. Here, only data from the central triple probe 3 is shown. The data set is chosen from a set of experiments in which conditions in forward and reversed magnetic field were reasonably matched (heating power and line integrated density agree within 15%). ECRH power varies between 2 MW for the lower density experiments to 5 MW for the higher density experiments, which does not affect this study as ECRH power has been shown to not significantly alter the SOL profiles in Standard configuration [40], see the appendix in section A.3. For all experiments, the toroidal plasma current amplitude was kept at $I_p < 3$ kA via electron cyclotron current drive [37] to ensure comparable SOL magnetic geometry. The reciprocating probe was inserted as deep as possible in each scenario without overheating due to the plasma heat loads. Hence, at lower densities, the probes were inserted closer to the LCFS, while high density experiments allowed only for less deep insertion.

The T_e profiles do not show a substantial variation over the scanned density range. A consistently higher electron temperature ($\Delta T_e \sim$10–20 eV) is observed in forward field direction over the entire profile. Generally, these T_e profiles do not show the hollowness of previous investigations [7, 11, 31, 32] as those earlier experiments were performed at slightly higher iota, where the 5/5 island chain is located radially further inside the plasma and therefore less intersected by the divertor. This is the same phenomenon as in the *High Mirror*

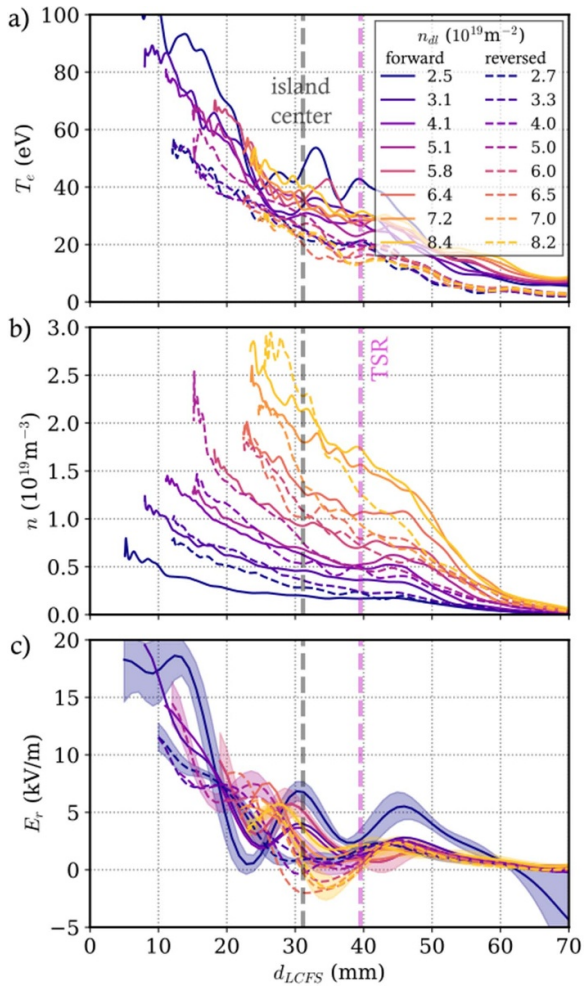

Figure 7. Radial profiles of T_e, n, E_r taken by reciprocating probes in forward (solid) and reversed (dashed) magnetic field operation in *Standard* configuration.

configuration in figure 4, where the local peaks at the TSR only manifest at increased plasma currents. In the 2024/2025 campaign of W7-X, the island chain was situated radially further outside as no 'iota correction' was applied to the planar coils [41] and the plasma current was kept small (below 3 kA). Thus, a larger part of the island is intersected by the divertor, and notably there is no confined region around the O point [37] in the MPM FoV.

The SOL density profiles show a clear correlation of SOL density to line integrated density and a systematic dependence on field direction: in forward direction (solid lines), SOL density profiles show a characteristic shoulder in the TSR at $d_{\mathrm{LCFS}} = 40$–50 mm. At the lowest core densities (blue), the SOL density profiles is remarkably flat across several cm. For higher core densities (orange), the SOL density profile in the island develops increasingly steep gradients, while a shoulder shape in the TSR still persists. In reversed field (dashed lines), in contrast, SOL density profiles exhibit a more similar decay length over the entire profile, with no or only weak density shoulder formation at the TSR. In a quantitative comparison, at low core densities (blue), higher SOL densities are observed in reversed field towards the LCFS, while at high core densities (orange) higher SOL densities are found in forward field, particularly around the TSR boundary.

It is interesting to note that the density gradients at the island center and in the outer part of the TSR become much steeper towards higher core densities, which could affect turbulent cross-field transport. The role of turbulent transport in these experiments will be briefly touched in section 5.

4.2. SOL profiles - high mirror configuration

Similar measurements have been conducted in the *High Mirror* configuration, which also features a 5/5 island chain forming the island divertor, while the interaction regions of islands and divertor plates are different [5]. A comparison of approximately matched discharges in forward and reversed magnetic field in figure 8 again shows consistently higher electron temperatures in forward magnetic field, as well as higher SOL densities in forward field up to line integrated densities of $n_{\mathrm{dl}} = 6.5 \times 10^{19}$ m^{-2}. The central triple probe 3 in figure 8(*b*) does not exhibit the clear TSR density shoulder as in *Standard* configuration in figure 7. However, examination of the density profiles from all five triple probes (see locations in figure 8(*e*) reveals considerable vertical (poloidal) density gradients, with the gradient direction and its radial localization depending on the magnetic field direction. In figure 8(*c*), in forward field the uppermost probe (probe 1) features the highest density and signs of a shoulder formation in the TSR1 region, and the lowermost probe (closest to the island O point) features the smallest density. In reversed field, this poloidal density gradient flips: the uppermost probe has the smallest density and the lowermost probe has the highest density. The five density profiles of each dataset are displayed in a smoothed interpolated 2D map in figure 8(*f*)) to better visualize the poloidal density gradient. The same behavior is found at a lower heating power in figure 8(*d*), where the level of asymmetry as smaller. There, the lowest probe shows similar values between forward and reversed field, while the upper probes exhibit an increase / decrease, depending on field direction. Generally, this behavior is universal across a large number of measurements in the *High Mirror* configuration.

4.3. Divertor target conditions

With the presence and effect of drift flows in the SOL being indicated in the previous subsections, it is obvious to investigate the effects on the divertor. As divertor heat flux data from the recent W7-X campaigns is still under final investigation, we here focus on divertor Langmuir probes.

Two poloidal probe arrays are installed across the horizontal divertor targets of the upper and lower divertor in module 5 of W7-X in stellarator-symmetric positions [42]. The divertor densities from a similar separatrix density scan to the previous section are presented in figure 9 for the probe closest to the strikeline (left column) and the probe at the TSR boundary (right column). For each probe position, densities in upper and lower divertor and in forward and reversed magnetic field direction are given. In all cases, and at both probe positions, divertor density increases approximately linearly with

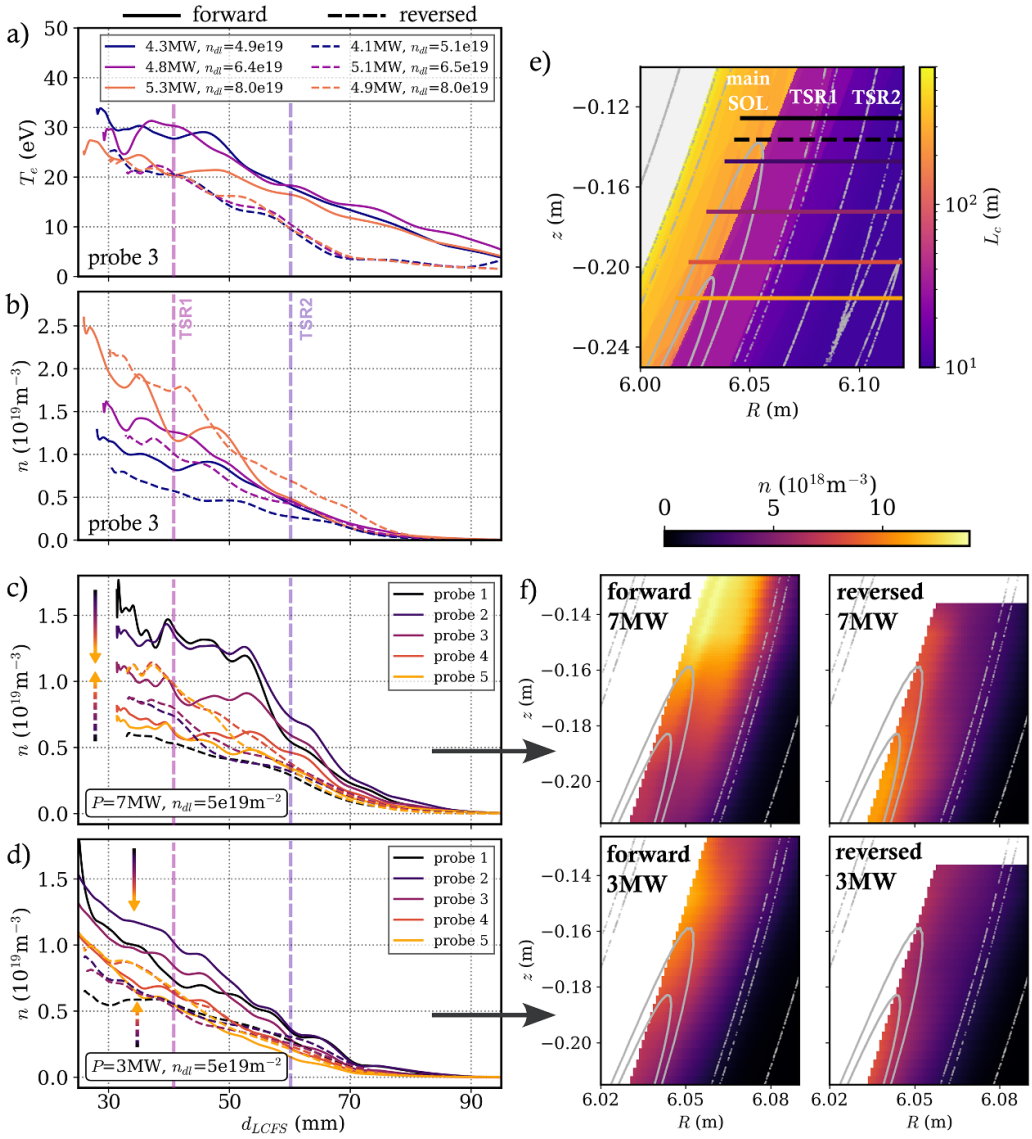

Figure 8. Radial profiles of T_e (*a*) and n (*b*)–(*d*) in the *High Mirror* configuration in forward and reversed field. (*a*) and (*b*) compare T_e, n profiles for the center probe 3 in matched pairs of experiments. (*c*) and (*d*) show density profiles for all five probes for two example discharges at different heating power. (*e*) shows the magnetic structure in the MPM region and the paths of the five triple Langmuir probes. Here, TSR1 denotes the purple region with $L_c \approx 30$ m and TSR2 the outer, more blue region with $L_c < 15$ m. Density profiles of (*c*) and (*d*) are interpolated onto a 2D plane in (*f*) to better visualize the poloidal density gradient.

core density. However, the slope of the increase depends on the magnetic field direction and the distinction between upper and lower divertor, indicating the potential role of drift effects. Further, the slope is larger for the TSR boundary position: over a factor of 4 in core density, the TSR density increases by up to an order of magnitude.

To make the up-down disparity more clear, the ratio of density in the upper vs. lower divertor for the two probe positions is shown in the bottom row, similar to the results in [9] for the *Low Iota* configuration. The vertical axis is scaled logarithmically, such that a certain density ratio has the same distance from the ratio $= 1$ line in both directions. At the strikeline, higher divertor densities are found in the upper divertor in forward field, and in the lower divertor in reversed field. The density ratio is ≈ 1.5 in both cases and does not significantly depend on core plasma density. At the TSR boundary, highly asymmetric divertor densities are found at low core plasma densities, with a ratio of up to a factor of 10 in forward field: higher densities are found in the lower divertor in forward field and in the upper divertor in reversed field. The asymmetry between TSR density in upper and lower divertor decreases towards higher core plasma densities.

4.4. Discussion of drift flow impact on SOL parameters

Interpreting the results presented in the previous subsections in view of the simplified drift flow picture from figures 1(*c*) and (*d*) yields qualitative agreement in multiple aspects:

In the *Standard* configuration in figure 7, higher densities in the TSR in forward field are observed and expected, as the

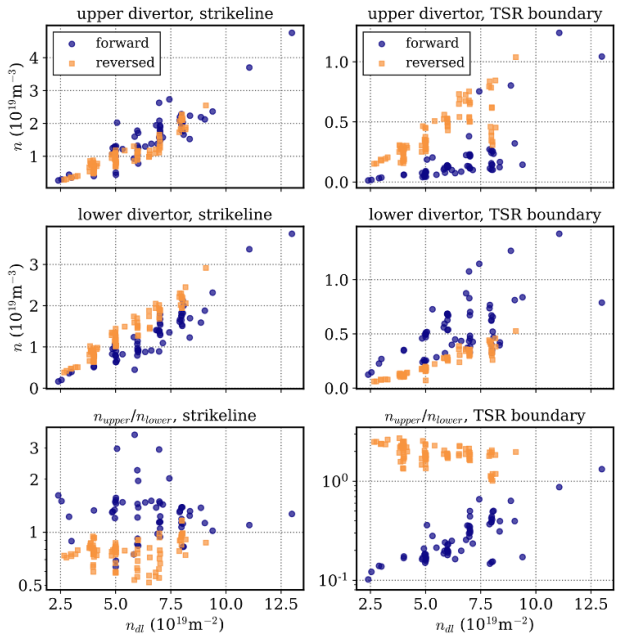

Figure 9. Plasma density from divertor Langmuir probes at the strikeline (left column) and the TSR boundary (right column) as a function of line-integrated density in *Standard* configuration. In the bottom row, the density ratio between upper and lower divertor is plotted in a log scale.

generally positive electric field (bottom panel of figure 7) convects plasma via $E \times B$ transport towards the TSR in the 'upper' half of the island, so that the consequences manifest in the TSR part that is probed by the MPM. In reversed field, E_r also exhibits mostly positive values, resulting in downwards $E \times B$ transport (see figure 1(*d*)), towards the 'lower' half of the island below the O point, i.e. away from the TSR part that is probed by the MPM. While the E_r profiles have a rather complicated shape, the density dependence in forward field shows on average smaller E_r for higher densities, which is qualitatively consistent with the decreasing flow velocities in figure 6(*a*) but is not clearly reflected in the SOL density profiles.

In the *High Mirror* configuration in figure 8(*f*), a field-direction dependent poloidal density gradient is observed in the SOL. The direction of this density gradient is consistent with GPI showing $E \times B$ drifts pointing upwards in forward field (figure 5(*b*)) and downwards in reversed field direction (figure 6(*b*)), assuming that the flows remain within the islands and do not move around the entire LCFS. The fact that the density gradient is smaller at lower heating power agrees with $\approx 20\%$ lower drift velocities at 3 MW compared to 7 MW as reported by GPI. However, the average radial profile shape does not vary a lot between the different heating levels, see also appendix A.3.

The up-down asymmetries of the divertor density in figure 9 agree with the simplified drift flow picture sketched in figure 1(*c*), where $E \times B$ convection is directed towards the strikeline in the upper divertor in forward field and towards the strikeline in the lower divertor in reversed field, and the opposite behavior for the TSR: drifts would point into the TSR in the upper divertor in reversed field and into the TSR in the lower divertor in forward field.

The observation of decreasing asymmetry towards higher plasma densities is qualitatively similar to the *Low Iota* results in [9] and also qualitatively agrees with reduced drift flow velocities (figure 6). However, in a quantitative comparison, the drift flow velocities only slightly decrease while the asymmetry decreases much more strongly. Several other issues remain unclear: In the TSR, the up-down asymmetry is much stronger in forward field than in reversed field. This might be caused by different error field correction used in forward and reversed field [38] and generally residual error fields beyond the best available compensation [38]. However, error fields cannot generally cause the observed up-down asymmetries as they persist in error field scans with different settings.

Both the lack of core density dependence of the up-down asymmetry at the strikeline and the very strong scaling of TSR density with core density are unexpected . These observations indicate that the simplified drift picture from figure 1(*c*) is too crude for assessment of the 3D transport. Especially the latter observation hints at further perpendicular transport processes (that are not field-direction dependent) causing the TSR density build-up. In the following section, turbulent transport and its potential role for transport into the TSR density is explored.

5. Perpendicular transport beyond drift flows

Motivated by the divertor probe results indicating increased perpendicular transport into the TSR at high core densities beyond drift flows, this section briefly explores turbulence measurements with the MPM reciprocating probes. We consider the dataset from the forward field experiments in figure 7 as the probe head was configured for turbulence measurements in these experiments, i.e. contained a 3-pin poloidal array of a central ion saturation current pin (giving a proxy for density fluctuations) and two floating probes (giving an estimate for the fluctuating poloidal electric field) [14].

The resulting profiles in figure 10 show that fluctuations and turbulent transport linearly increase with SOL and core plasma density. The data from the probe plunges was cut in 5 ms long windows, such that the probe does not move more than its size (2 mm pin length) in each window. First, figure 10(*a*) repeats the SOL density profiles from figure 7. The ion saturation current ($I_{\mathrm{i,sat}}$) fluctuations (standard deviation in the 2–100 kHz range) from a constantly negatively biased pin are presented in figures 10(*b*) and (*c*) (same quantity but normalized to the mean $I_{\mathrm{i,sat}}$ in the respective time window). $I_{\mathrm{i,sat}}$ fluctuation amplitudes mostly decrease monotonically across the SOL but show a local flattening at the TSR boundary. Hence, the normalized fluctuation levels in figure 10(*c*) show a minimum at that position. However, the overall normalized fluctuation amplitude does not vary more than a factor of 2 over the entire profile up to $d_{\mathrm{lcfs}} = 60$ mm (values increase beyond that due to vanishingly small mean $I_{\mathrm{i,sat}}$ levels).

In the core plasma density scan indicated by marker color, the $I_{\mathrm{i,sat}}$ fluctuations increase approximately linearly with core density as shown in figure 10(*b*). As the SOL density increases

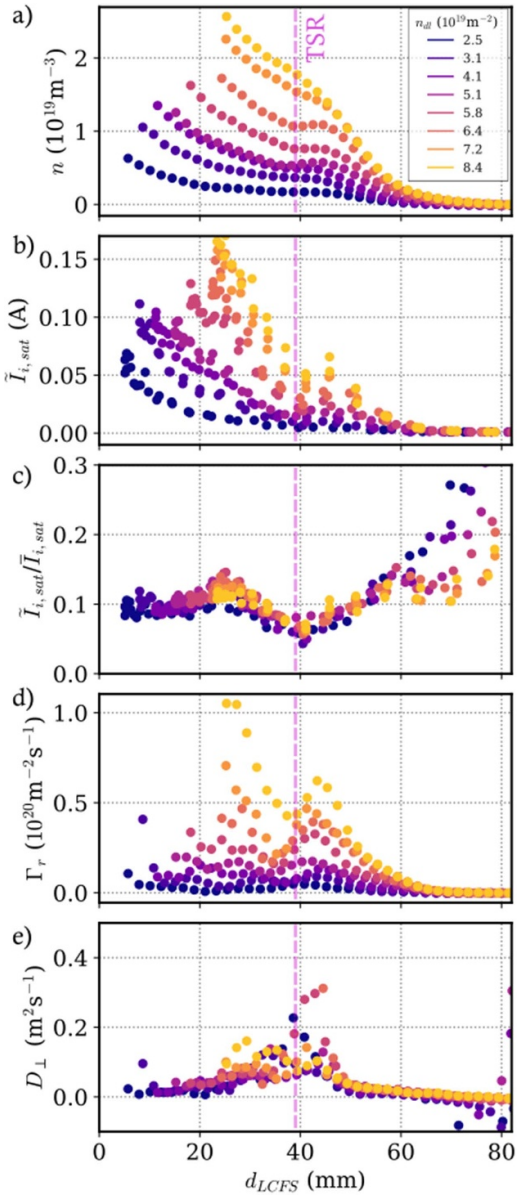

Figure 10. Radial profiles determined by MPM probes for the forward field dataset from figure 7. Each data point represents a 5 ms window. Fluctuations in the spectral range 2–100 kHz are considered. (*a*) Plasma density, (*b*) $I_{\mathrm{i,sat}}$ fluctuations (standard deviation), (*c*) $I_{\mathrm{i,sat}}$ fluctuations normalized to each window's mean value, (*d*) turbulent radial particle flux Γ_r, (*e*) perpendicular diffusion coefficient $D_\perp = -\Gamma_r \nabla n$.

with core density in a similar fashion (figure 10(*a*)), the normalized fluctuation amplitudes in figure 10(*c*) do not show any core density dependence.

The turbulent radial particle flux $\Gamma_r = \tilde{n}\tilde{v_r}$ [14] in figure 10(*d*) also increases as a function of core density. Such increased radial particle flux at high core densities is expected to contribute to heat and particle transport into the TSR and might explain the increased TSR densities at high core densities in figures 9(*a*) and (*b*). Detailed fluctuation analysis shows that the density dependence of Γ_r mostly stems from the $I_{\mathrm{i,sat}}$ fluctuations in figure 10(*b*), while the cross-phase between $I_{\mathrm{i,sat}}$ and V_{f} as well as $I_{\mathrm{i,sat}}$ and v_r does not change significantly across these density scan experiments. Hence, the nature of turbulence does not change here as a function of separatrix density, as was reported in tokamaks [15].

The perpendicular diffusion coefficient profile presented in figure 10(*e*) also does not show a significant dependence on core density, as both Γ_r and the density gradient ∇n increase similarly in the core density scan (the normalized density gradient $\nabla n/n$ also remains unaffected by the core density scan). The shape of the Γ_r and $D_\perp$ profile is however difficult to interpret. The highest $D_\perp$ values are observed at the TSR boundary, where the density gradients are rather small. Still, values of $D_\perp \approx 0.1\,\mathrm{m^2\,s^{-1}}$ are rather small compared to typical modeling assumptions [22]. The overall profile shape of Γ_r (and thus $D_\perp$), and in particular the small values of these quantities close to the LCFS, are not understood at this point and will be investigated in more detail in a future analysis.

6. Summary and conclusion

Bi-normal drift flows with velocities of several km s^{-1} are ubiquitously observed in the W7-X island divertor SOL using GPI and reciprocating probes. These drift flows provide an efficient transport channel in the island divertor SOL, as they short-cut the parallel direction: due to the small magnetic pitch angle in the islands, parallel transport on the magnetic island field lines has to take an up to 1000 times longer path compared to the transport on the island flux surfaces. The velocity and distribution of drift flows is highly sensitive to the radial position of the SOL magnetic islands.

In a simplified picture of the effect of such drift flows, the expected plasma convection by drifts agrees with experimentally observed features of SOL and divertor density profiles that are not reproduced by current models. In particular, the experimentally indicated drift transport into (away from) the TSR of the divertor is expected to cause significant density increase (decrease) in the TSR for upper (lower) divertors in forward field direction; and vice versa for reversed field. Such up-down asymmetries are observed particularly clearly in the TSR part of the divertor plasma. Further, SOL density profiles show qualitatively agreeing profile shapes, with clear density shoulders in the TSR appearing only in forward field direction, and poloidal density gradients in the island agreeing with the $E \times B$ convection. While the full picture of the interplay between drift flow transport and other processes in the 3D SOL is more complex and not yet globally understood, these observations clearly indicate the key role of drift flows in causing transport into the TSR, both at the divertor and in the SOL. The findings in this paper therefore emphasize the relevance of drift flows for understanding and modeling transport processes in the W7-X island divertor. Modeling tools for future stellarator reactors need to include drift physics in order to correctly predict divertor operation scenarios.

In detail, many questions remain open: Due to diagnostic coverage limitations, there is still no global validation of observed drift flows (from GPI) and the underlying electric fields (from MPM probes). Furthermore, while the drift flow velocities slightly decrease for higher plasma densities, the

up-down density asymmetry at the divertor decreases much more strongly. The strong increase of absolute TSR density (up-down symmetric) at high core densities cannot be explained by bi-normal drift flows. The role of turbulence has been explored here and shows increasingly high density gradients and turbulent particle fluxes at high core densities, but no transition towards a qualitatively different turbulence regime was observed. Given the 3D distribution of plasma parameters in the SOL, the potential limitation from only measuring turbulence in the radial and drift flows in the bi-normal direction remains to be explored in future investigations.

Acknowledgments

This work has been carried out within the framework of the EUROfusion Consortium, funded by the European Union via the Euratom Research and Training Programme (Grant Agreement No. 101052200 — EUROfusion). Views and opinions expressed are however those of the author(s) only and do not necessarily reflect those of the European Union or the European Commission. Neither the European Union nor the European Commission can be held responsible for them.

Appendix

A.1. Magnetic configurations

The *Standard* and *High Mirror* configuration are the two most commonly run configurations in W7-X. Both operate in island divertor mode with a 5/5 island chain in the SOL due to $\iota/2\pi = 1$ at the LCFS. The magnetic structure of the SOL (Poincare plots and target-to-target connection length) for both configurations is presented in figure 11 for the cross section where GPI and MPM are installed (in different stellarator-symmetric modules). Both configurations share the same main features and SOL regions described in section 2. However, as a consequence of the slightly different shape of the plasma and the magnetic island chain, the divertor targets are intersected at different positions, resulting in a different connection length pattern in the SOL.

For both configurations, a reconstruction for a finite plasma current of 6 kA is shown in comparison to the vacuum case (relevant to figure 4). The plasma current increases the iota profile, moving the islands inwards, away from the targets [31, 37].

A.2. List of experiments used in this work

For figures containing data from multiple experiments, the list of experiment programs is given below.

- *Standard* configuration, forward field (figures 6(*a*), 7, 9 and 10): 20241127.22, 20241127.24, 20241127.25, 20241127.29
- *Standard* configuration, reversed field (figures 7 and 9): 20250304.60, 20250304.61, 20250304.73, 20250304.79, 20250304.81, 20250304.83, 20250304.86, 20250304.89

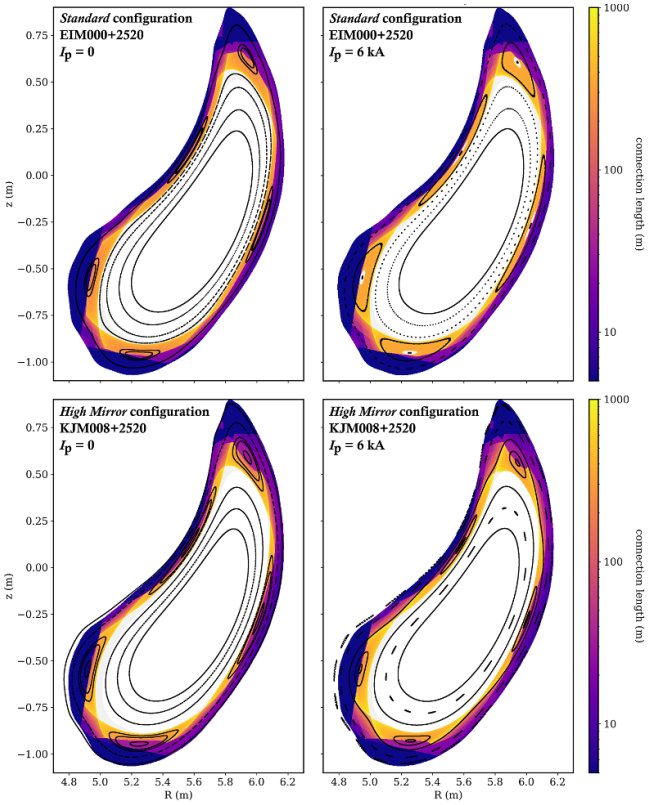

Figure 11. Magnetic structure of the *Standard* (top row) and *High Mirror* (bottom row) configuration for the vacuum case (left) and with a toroidal plasma current of 6 kA (right). Poincare plot is shown in black, target–target connection lengths are color coded. In all cases, an 'iota correction' offset of 250 A has been applied to the planar coils to account for coil deformation [41].

- *High Mirror* configuration, forward field (figure 8): 20241120.20, 20241120.21, 20241120.29
- *High Mirror* configuration, reversed field (figures 6 and 8): 20250305.75, 20250305.79, 20250305.82

A.3. Effect of ECRH power on SOL parameters

In order to assess the effect of operation parameters on the SOL plasma conditions, a systematic scan of ECRH power and line-integrated density has been conducted in *Standard* configuration in forward field direction. In each experiment program, P_{ECRH} was varied between 5 MW and 3 MW while the density was kept stable for the entire discharge. The ECRH system was set such that a small current drive counteracts the bootstrap current evolution, resulting in approximately constant net plasma current and therefore constant island position [37]. All plasmas were well attached to the divertor with radiated power levels $P_{\mathrm{rad}} < 1$ MW.

The resulting electron temperature and density profiles measured by the center triple probe of the MPM are presented in figure 12. Each color represents one line-integrated density level, while the different shadings of each color correspond to the P_{ECRH} scan. Overall, no substantial effect of P_{ECRH} is observed, as both T_e and n do not vary a lot under P_{ECRH} changes. Upon close inspection, a very small effect

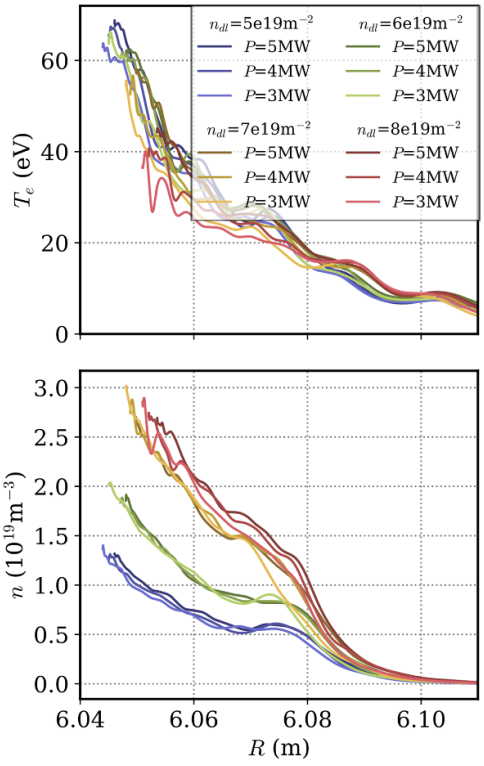

Figure 12. Radial profiles of T_e and n taken in a systematic scan of heating power and core plasma density from experiments 20241127.[24–27] in *Standard* configuration, forward magnetic field direction.

towards lower T_e and n for lower heating power is observed, see e.g. the blue density profiles for $n_{dl} = 5 \times 10^{19}\,\mathrm{m}^{-2}$. Also, for the higher core densities of $n_{dl} = 8 \times 10^{19}\,\mathrm{m}^{-2}$, $n_{dl} = 7 \times 10^{19}\,\mathrm{m}^{-2}$ (yellow, red data), T_e slightly (but significantly) decreases in the 3 MW cases.

Figure 12 further illustrates the role of core (and therefore separatrix) plasma density for the SOL. While T_e remains generally unaffected, the SOL density increases significantly with n_{dl}. Similar to figure 7, a local density peak (at low n_{dl}) and a density shoulder (at high n_{dl}) are observed at the TSR boundary ($R \approx 6.075\,\mathrm{m}$).

The lack of impact of P_{ECRH} is unexpected, as the different heating power levels correspond directly to different levels of power in the SOL. Across the general W7-X database of MPM probe measurements, T_e profiles show considerably stronger variation than in figure 12 in nominally similar experiment, but machine operation details vary in detail over the campaign. The question of where the heating power ends up in the SOL and the role of plasma operation settings (particularly: ECRH settings) remains to be addressed urgently in future experiments.

A.4. The uppermost Langmuir probes on MPM probe heads

Data from the uppermost pins on the MPM probe head (design see [7]) often, regardless of magnetic configuration, appear to be outliers: In figure 3, triple probe 1 shows consistently very small temperatures in the main SOL, although the density profiles (which are determined based on the ion saturation current and depend on $T_e^{-0.5}$ via $n \sim I_{i,sat}/c_s$ with $c_s \sim \sqrt{T_e}$) fit well with the other probes results. This behavior is very universal in *Standard* configuration across hundreds of measurements. In figure 8(*d*), triple probe 1 does not follow a clear density gradient along probe position in forward field. In figure 4, triple probe 1 shows higher T_e compared to all other probes, and, as a result of $n \sim I_{i,sat} T_e^{-0.5}$ at similar $I_{i,sat}$ values, lower density.

After every possible measure to rule out a technical error (cables, electronics) was attempted to no avail, the position of the uppermost triple probe was changed to a 12 mm vertically lower position for the majority of the 2025 experiment campaign, see the dashed black line in figure 8(*e*). After this change, the results of the uppermost probe were much better in line with the other probes. All reversed field experiments were conducted in the 2025 campaign with the changed probe 1 position, while all forward field experiments in this paper were conducted in the 2024 campaign with the 'original' probe 1 position.

The reason for the effect of triple probe vertical position is still unclear. One reason might be highly localized plasma effects, e.g. electric currents in the SOL. The consistent observation of localized V_f peaks on the uppermost floating probes (see figure 4 and results in [7]) would support such a conjecture. Further, the uppermost probes consistently exhibited by far stronger carbon deposition and erosion compared to the majority of the probe head.

ORCID iDs

Carsten Killer 0000-0001-7747-3066
Dario Cipciar 0000-0002-3798-9524
Arun Pandey 0000-0003-4423-3140
Valeria Perseo 0000-0001-8473-9002
Floris Scharmer 0009-0005-2310-5731
Seung Gyou Baek 0000-0001-8029-3525
Olaf Grulke 0000-0001-7879-8671
David Matthew Kriete 0000-0002-3657-2911
Felix Reimold 0000-0003-4251-7924
Adrian von Stechow 0000-0003-0277-4600

References

[1] König R. *et al* 2002 *Plasma Phys. Control. Fusion* **44** 2365
[2] Feng Y., Sardei F., Grigull P., McCormick K., Kisslinger J. and Reiter D. 2006 *Nucl. Fusion* **46** 807
[3] Pedersen T.S. *et al* (the W7-X-Team) 2022 *Nucl. Fusion* **62** 042022
[4] Feng Y. (the W7-X-team) 2022 *Plasma Phys. Control. Fusion* **64** 125012
[5] Gao Y. *et al* (the W7-X team) 2020 *Nucl. Fusion* **60** 096012
[6] Kraemer-Flecken A. *et al* 2019 *Plasma Phys. Control. Fusion* **61** 054003
[7] Killer C., Cipciar D., Baek S.G., Ballinger S.B., Stechow A.v., Terry J.L., Grulke O. and (the W7-X Team) 2025 *Nucl. Fusion* **65** 056026
[8] Ballinger S., Baek S., von Stechow A., Terry J. and Killer C. (W7-X-Team) 2023 Gas puff imaging of filament dynamics in the SOL of W7-X *Presented at 65th APS-DPP Conf. (Denver, Colorado, 30 October–3 November 2023)*

[9] Kriete D. *et al* (the W7-X Team) 2023 *Nucl. Fusion* **63** 026022
[10] Hammond K.C. *et al* (the W7-X team) 2019 *Plasma Phys. Control. Fusion* **61** 125001
[11] Flom E. *et al* (W-X Team) 2024 Observation of a drift-driven transport regime in the island divertor of Wendelstein 7-X (arXiv:2312.01240)
[12] Killer C., Shanahan B., Grulke O., Endler M., Hammond K. and Rudischhauser L. (the W7-X Team) 2020 *Plasma Phys. Control. Fusion* **62** 085003
[13] Csillag B., Zoletnik S., Killer C., Vecsei M., Anda G., Dunai D., Hegedus S., Refy D., Nagy D., Otte M. and (the W7-X Team) 2023 *Nucl. Fusion* **64** 016017
[14] Killer C., Narbutt Y. and Grulke O. (the W7-X Team) 2021 *Nucl. Fusion* **61** 096038
[15] Carralero D. *et al* 2017 *Nucl. Fusion* **57** 056044
[16] Grulke O. 2026 Overview of W7-X high performance operation *Nucl. Fusion* accepted (https://doi.org/10.1088/1741-4326/ae5f32)
[17] Perseo V. 2025 Increased power operation with water-cooled divertors at W7-X *IAEA Technical Meeting on Divertors* (*Vienna, Austria*, *28–31 October 2025*)
[18] Coelho A., Loizu J., Ricci P. and Tecchiolli Z. 2024 *Nucl. Fusion* **64** 076057
[19] Tork T., Reimold F., Bold D., Shanahan B., Dudson B., Stegmeir A. and Manz P. 2025 A BOUT++ transport model for island diverted stellarators including drifts *67th Annual Meeting of the APS Division of Plasma Physics* (*Long Beach, CA*, *17–21 November 2025*)
[20] Stegmeir A., Finkbeiner M.E., Pitzal C., Geiger J. and Jenko F. 2026 *Comput. Phys. Commun.* **318** 109874
[21] Feng Y. *et al* (the W7-X Team) 2021 *Nucl. Fusion* **61** 106018
[22] Bold D., Reimold F., Niemann H., Gao Y., Jakubowski M., Killer C., Winters V.R. and (the W7-X Team) 2022 *Nucl. Fusion* **62** 106011
[23] Bold D., Reimold F., Niemann H., Gao Y., Jakubowski M., Killer C., Winters V.R., Maaziz N. and (the W7-X Team) 2024 *Nucl. Fusion* **64** 126055
[24] Perseo V., Effenberg F., Gradic D., König R., Ford O., Reimold F., Ennis D., Schmitz O. and Sunn Pedersen T. (the W7-X Team) 2019 *Nucl. Fusion* **59** 124003
[25] Effenberg F. *et al* (the W7-X Team) 2017 *Nucl. Fusion* **57** 036021
[26] Feng Y. *et al* (the W7-X Team) 2021 *Nucl. Fusion* **61** 086012
[27] Winters V. *et al* (the W7-X Team) 2024 *Nucl. Fusion* **64** 126047
[28] Geiger J., Beidler C.D., Feng Y., Maaßberg H., Marushchenko N.B. and Turkin Y. 2015 *Plasma Phys. Control. Fusion* **57** 014004
[29] Feng Y., Kobayashi M., Lunt T. and Reiter D. 2011 *Plasma Phys. Control. Fusion* **53** 024009
[30] Zhang D. *et al* (the W7-X Team) 2025 *Nucl. Fusion* **65** 096032
[31] Killer C. *et al* (the W7-X Team) 2019 *Plasma Phys. Control. Fusion* **61** 125014
[32] Barbui T. *et al* (the W7-X Team) 2020 *Nucl. Fusion* **60** 106014
[33] Baek S., Ballinger S., Grulke O., Killer C., von Stechow A., Terry J., Scharmer F. and Shanahan B. 2025 *Nucl. Mater. Energy* **43** 101937
[34] Bozhenkov S. *et al* (W7-X Team) 2020 *Nucl. Fusion* **60** 066011
[35] Terry J.L. *et al* (W-X Team) 2024 *Rev. Sci. Instrum.* **95** 093517
[36] Neuner U. *et al* (the Wendelstein 7-X Team) 2021 *Nucl. Fusion* **61** 036024
[37] Gao Y. *et al* (W7-X Team) 2019 *Nucl. Fusion* **59** 106015
[38] Gao Y. 2025 Observation and control of 3D heat flux on the plasma facing components in Wendelstein 7-X *Preprint: 2025 IAEA Fusion Energy Conf.* (*Chengdu, China*, *13–18 October 2025*)
[39] Cipciar D., Adamek J., Killer C., Matthew Kriete D., Winters V., Perseo V., Grulke O., Hua J. and Knieps A. (the W7-X Team) 2025 *Plasma Phys. Control. Fusion* **67** 115029
[40] Kharwandikar A. 2025 Power exhaust investigations in the W7-X island divertor *PhD Thesis* University of Greifswald, Greifswald
[41] Lazerson S.A. *et al* (W7-X Team) 2019 *Nucl. Fusion* **59** 126004
[42] Pandey A. *et al* (the W7-X Team) 2024 *Rev. Sci. Instrum.* **95** 043503